SRRF 'n' TIRF - FCS: Simultaneous spatiotemporal super-resolution microscopy

Jagadish Sankaran[1,*], Harikrushnan Balasubramanian[1,*], Wai Hoh Tang[2], Xue Wen Ng[1], Adrian Röllin[2], Thorsten Wohland[1,3]

[1]Department of Biological Sciences and NUS Centre for Bio-Imaging Sciences, National University of Singapore, 14 Science Drive 4, 117557 Singapore

[2]Department of Statistics and Applied Probability, National University of Singapore, 6 Science Drive 2, Singapore 117546

[3]Department of Chemistry, National University of Singapore, 3 Science Drive 3, 117543 Singapore

*contributed equally to the work

Abstract

Super-resolution microscopy and single molecule fluorescence spectroscopy require mutually exclusive experimental strategies optimizing either time or spatial resolution. To achieve both, we implement a GPU-supported, camera-based measurement strategy that highly resolves spatial structures (~60 nm), temporal dynamics (≤ 2 ms), and molecular brightness from the exact same data set. Using epidermal growth factor receptor (EGFR), we demonstrate that pixel-wise correlation of parameters obtained from different techniques provides new biological knowledge.

Key Words

Super-resolution, Imaging fluorescence correlation spectroscopy, Number and brightness analysis, Super-resolution radial fluctuations, FCS diffusion law, Epidermal growth factor receptor

Full knowledge of a biological system requires not only information on its spatial structure but also its temporal dynamics. However, the acquisition of structure and dynamics requires complementary, often mutually exclusive optimization strategies[1]. Spatial resolution depends on the number of photons collected and thus sets a lower limit on acquisition time. Molecular dynamics requires acquisition times shorter than the dynamics of interest and thus sets an upper limit. Since these two limits, in general, do not lead to an overlap region, the combination of spatiotemporal super-resolution microscopy has remained a challenge. Attempts in the past either restrict time resolution[2,3], require specialized instrumentation[4,5] or sample labeling[6,7].

While simultaneous multi-parametric fluorescence detection (MFD) has been established for point-measurements[8,9], such attempts in an imaging mode have been hampered by lack of strategies that can bridge the limitations imposed by spatial and temporal resolution requirements and by the computationally expensive data evaluation procedures required to treat the large data sets. Here, we overcome these problems by acquiring images with high sensitivity and high-speed using commercially available cameras and GPU-based data processing. The resulting datasets are evaluated by a combination of spectroscopy and super-resolution techniques that include: imaging fluorescence correlation spectroscopy (Imaging FCS)[10,11] to measure dynamics; FCS diffusion law analysis to obtain information about the dynamic sub-resolution molecular organization[12]; Number and Brightness analysis (N&B)[13] to determine oligomerization or aggregation states; and super-resolution radial fluctuation microscopy (SRRF)[14] to obtain super-resolved images (Fig. S1). Using a recently published GPU-based algorithm for SRRF[14] and a newly developed GPU accelerated version of Imaging FCS (Fig. S2), an ImageJ plugin developed in our group, we achieve measurements with high spatial information (~60 nm) and temporal dynamics (≤ 2 ms) from the exact same data within ~5 min, including measurement time (Figs. S3-S5, Tables 1, S1-S2).

As a proof-of-principle, we analyzed EGFR receptor dynamics and organization and the cytoskeletal structure on CHO-K1 cell membranes using a commercially available total internal reflection fluorescence (TIRF) microscope. We recorded image stacks of mApple labelled EGFR (EGFR-mApple) and LifeAct[15], an actin binding protein labelled with EGFP, on whole cells using EMCCD and sCMOS cameras for detection (50,000 frames at 2 ms time resolution covering areas as large as 128×128 pixels). For the simultaneous acquisition of the mApple and EGFP signals on two halves of one camera, we used a wavelength-based image splitter.

A comparison of the structure and the dynamics of LifeAct in the green channel alone shows clear correlations (Fig S6). The diffusion coefficient on the fibres was found to be 0.77 ± 0.53 $\mu m^2/s$. The region between fibres contain only few lifeact particles[16]. Using 4×4 pixel binning to improve the signal-to-noise ratio (SNR), the diffusion coefficient was 2.89 ± 3.20 $\mu m^2/s$, indicating free diffusion of LifeAct or LifeAct bound to globular actin[15] (Fig. S7). The measured optical resolution of SRRF was in the range of 78 - 120 nm (Table S3). Using SRRF to localize the cytoskeleton more precisely, we can select only those pixels in the FCS diffusion coefficient map that lie directly on top of the cytoskeleton fibres and are thus less influenced by freely diffusing LifeAct. After using the SRRF image as a selection mask, the diffusion coefficient on the fibre was found to be 0.80 ± 0.39 $\mu m^2/s$ whereas in neighbouring pixels it was found to be 0.75 ± 0.66 $\mu m^2/s$. (Fig. S8). SRRF selection thus improves the estimated diffusion coefficient precision by about a factor 1.4. Furthermore, the FCS results corroborate the SRRF resolved positions of the

fibres as there is a correlation between the SRRF actin fibre position and the SNR of the FCS data (Fig. S8, Table S4).

The full extent of the information however is gained when analyzing both wavelength channels. To investigate the interrelation between the actin cytoskeleton structure, which is relatively static on the time scale of our measurements, and EGFR mobility and organization, which is highly dynamic, we optimized the signals by spatiotemporal binning for either FCS and FCS diffusion law, N&B (red channel, Figs. 1 a-d, Fig. S9) or SRRF (green channel, Figs. 1 e-g) analysis. SRRF analysis led to an improvement of the FWHM from 465 nm to 97 nm of actin fibres. In the whole cell, N&B analysis revealed that 63 ± 3 % of EGFR existed as apparent dimers (supplement). The diffusion coefficient was found to be 0.19 ± 0.15 $\mu m^2/s$ with a FCS diffusion law intercept of 2.58 s, indicating intermittent trapping of EGFR. The large error associated with the diffusion coefficient is attributed to the inherent heterogeneity in the cell membrane. The various factors contributing to the heterogeneity are investigated using a multi-parametric analysis.

EGFR-mApple expressing cells show both regions of uniform intensity and regions exhibiting visible clustering (Fig. 1a). Analysis of the regions of homogeneous brightness in the mApple channel by Imaging FCS and the FCS diffusion law resulted in a diffusion coefficient of D = 0.24 ± 0.16 $\mu m^2/s$ and a positive diffusion law intercept of 1.81 s (Fig. S10), indicating transiently trapped diffusion and possibly EGFR oligomerization or clustering[17]. The existence of oligomers is corroborated by N&B analysis of the same regions. EGFR-mApple showed a brightness intermediate between monomers and dimers (Fig. S9), suggesting that 18 ± 6% of receptors are found in dimers (Fig. S10), although we cannot exclude the existence of small amounts of higher oligomers[18]. When analyzing the regions with visible clusters present, we obtain a D = 0.11 ± 0.08 $\mu m^2/s$ (Fig. S10) via FCS. In this case, a simple dimer model is not reasonable anymore. A brightness value of 5.87 (average value of the cluster containing areas in Fig. 1 and S10) indicates that at least trimers, if not higher oligomers, are present.

The existence of preformed oligomers is consistent with literature with up to ~65% dimerization previously detected[18-20] in the same cell line. Diffusion law intercepts did not show a statistically significant difference when comparing areas where visible clusters or actin is present with areas where they were absent (Table S5, $p > 0.14$). This indicates that the domain partitioning of EGFR is primarily determined by EGFR-membrane interactions, possibly sub-resolution clustering and inter-EGFR interactions but independent of EGFR-actin interactions.

Since all evaluations stem from the exact same data set we overlap the parameter maps and pairwise analyze their scatter plots to determine the interdependence of protein location with its dynamics. We performed a logarithmic transformation of the entire dataset to identify power law scaling between parameters (Fig. 1h-m).

Using whole cell data, we find a negative correlation between particle brightness and diffusion coefficient (Pearson's correlation coefficient (R) = -0.34, Table S6 and Fig. 1h), indicating that brighter particles diffuse slower than dimmer particles. This is unexpected since membrane diffusion is only weakly dependent on size[21]. This implies either that EGFR oligomers are located in a more viscous membrane environment, e.g. lipid domains[22] or clathrin-coated pits, or that we detect multiple EGFR molecules in larger complexes[18,23,]. A negative correlation (R= -0.83) is also

seen between diffusion coefficient and the positive diffusion law intercept indicating that trapping is responsible for lower EGFR mobility as expected (Table S6).

Brightness and SRRF do not show any correlation (R = 0.00, Fig. 1 l), implying that clustering is not directly linked to the cytoskeleton. Similarly, we do not see any correlation between EGFR diffusion and cytoskeletal structures (R = -0.05, Fig. 1 m), unlike in the case of LifeAct. This also verifies our earlier observation that diffusion law intercepts are independent of the presence or absence of actin. As it has been shown previously that EGFR dynamics changes with cytoskeleton disruption[24], our observations suggest that it is not the static cytoskeleton itself that changes EGFR dynamics but that the influence is indirect and cytoskeleton coupling to the plasma membrane and resulting membrane changes are responsible for changes in EGFR dynamics[25]. Similar results were obtained by performing the experiment using sCMOS camera as a detector (Figs. S11-S13).

Living systems are highly dynamic with processes happening on spatial scales well below the optical diffraction limit and on time scales on the millisecond scale or faster. Therefore, the extraction of the maximum information available on biological processes requires the simultaneous acquisition of data with high spatiotemporal resolution. This poses particular problems to data recording and data evaluation strategies that allow data treatment in an acceptable time frame, ideally in real-time. We used GPU-based data evaluation and modern camera technology to optimize data evaluation of fluorescence microscopy images by selected spatial and temporal binning to extract multiple physicochemical parameters in parallel from a single data set, almost in real time, using standard and widely available instrumentation. Parameter correlations and the lack thereof provide information not available on sequentially acquired data due to the dynamical nature of biological samples as shown on the example of EGFR. This approach is easily extendable to other fluorescence parameters, does not require specialized instrumentation, and thus is immediately applicable to a wide range of situations.

1 Weigert, M. *et al.* Content-aware image restoration: pushing the limits of fluorescence microscopy. *Nature Methods* **15**, 1090-1097, doi:10.1038/s41592-018-0216-7 (2018).

2 Ashdown, G. W., Cope, A., Wiseman, P. W. & Owen, D. M. Molecular flow quantified beyond the diffraction limit by spatiotemporal image correlation of structured illumination microscopy data. *Biophysical journal* **107**, L21-23, doi:10.1016/j.bpj.2014.09.018 (2014).

3 Kisley, L. *et al.* Characterization of Porous Materials by Fluorescence Correlation Spectroscopy Super-resolution Optical Fluctuation Imaging. *ACS Nano* **9**, 9158-9166, doi:10.1021/acsnano.5b03430 (2015).

4 Leutenegger, M., Ringemann, C., Lasser, T., Hell, S. W. & Eggeling, C. Fluorescence correlation spectroscopy with a total internal reflection fluorescence STED microscope (TIRF-STED-FCS). *Optics express* **20**, 5243-5263, doi:10.1364/OE.20.005243 (2012).

5 Hedde, P. N. *et al.* Stimulated emission depletion-based raster image correlation spectroscopy reveals biomolecular dynamics in live cells. *Nature Communications* **4**, 2093, doi:10.1038/ncomms3093 (2013).

6 Manley, S. *et al.* High-density mapping of single-molecule trajectories with photoactivated localization microscopy. *Nature Methods* **5**, 155-157, doi:10.1038/nmeth.1176 (2008).

7 Strauß, S. *et al.* Modified aptamers enable quantitative sub-10-nm cellular DNA-PAINT imaging. *Nature Methods* **15**, doi:10.1038/s41592-018-0105-0 (2018).

8 Weidtkamp-Peters, S. *et al.* Multiparameter fluorescence image spectroscopy to study molecular interactions. *Photochemical & Photobiological Sciences* **8**, 470-480, doi:10.1039/B903245M (2009).

9 Esposito, A. & Venkitaraman, A. R. Enhancing Biochemical Resolution by Hyperdimensional Imaging Microscopy. *Biophysical journal* **116**, 1815-1822, doi:https://doi.org/10.1016/j.bpj.2019.04.015 (2019).

10 Kannan, B. *et al.* Spatially resolved total internal reflection fluorescence correlation microscopy using an electron multiplying charge-coupled device camera. *Anal. Chem.* **79**, 4463-4470, doi:10.1021/ac0624546 (2007).

11 Wohland, T., Shi, X., Sankaran, J. & Stelzer, E. H. K. Single Plane Illumination Fluorescence Correlation Spectroscopy (SPIM-FCS) probes inhomogeneous three-dimensional environments. *Opt. Express* **18**, 10627-10641 (2010).

12 Wawrezinieck, L., Rigneault, H., Marguet, D. & Lenne, P. F. Fluorescence correlation spectroscopy diffusion laws to probe the submicron cell membrane organization. *Biophysical journal* **89**, 4029-4042, doi:10.1529/biophysj.105.067959 (2005).

13 Unruh, J. R. & Gratton, E. Analysis of molecular concentration and brightness from fluorescence fluctuation data with an electron multiplied CCD camera. *Biophysical journal* **95**, 5385-5398, doi:10.1529/biophysj.108.130310 (2008).

14 Gustafsson, N. *et al.* Fast live-cell conventional fluorophore nanoscopy with ImageJ through super-resolution radial fluctuations. *Nature Communications* **7**, 12471, doi:10.1038/ncomms12471 (2016).

15 Riedl, J. *et al.* Lifeact: a versatile marker to visualize F-actin. *Nature Methods* **5**, 605-607, doi:10.1038/nmeth.1220 (2008).

16 Sankaran, J. *et al.* Single microcolony diffusion analysis in Pseudomonas aeruginosa biofilms. *npj Biofilms and Microbiomes* **5**, 35, doi:10.1038/s41522-019-0107-4 (2019).

17 Abulrob, A. *et al.* Nanoscale imaging of epidermal growth factor receptor clustering: effects of inhibitors. *The Journal of biological chemistry* **285**, 3145-3156, doi:10.1074/jbc.M109.073338 (2010).

18 Saffarian, S., Li, Y., Elson, E. L. & Pike, L. J. Oligomerization of the EGF receptor investigated by live cell fluorescence intensity distribution analysis. *Biophysical journal* **93**, 1021-1031, doi:10.1529/biophysj.107.105494 (2007).

19 Liu, P. *et al.* Investigation of the dimerization of proteins from the epidermal growth factor receptor family by single wavelength fluorescence cross-correlation spectroscopy. *Biophysical journal* **93**, 684-698, doi:10.1529/biophysj.106.102087 (2007).

20 Zanetti-Domingues, L. C. *et al.* The architecture of EGFR's basal complexes reveals autoinhibition mechanisms in dimers and oligomers. *Nature Communications* **9**, 4325, doi:10.1038/s41467-018-06632-0 (2018).

21 Saffman, P. G. & Delbrück, M. Brownian motion in biological membranes. *Proceedings of the National Academy of Sciences* **72**, 3111-3113, doi:10.1073/pnas.72.8.3111 (1975).

22 Sergé, A., Bertaux, N., Rigneault, H. & Marguet, D. Dynamic multiple-target tracing to probe spatiotemporal cartography of cell membranes. *Nature Methods* **5**, 687-694, doi:10.1038/nmeth.1233 (2008).

23 Nagy, P. *et al.* Activation-dependent clustering of the erbB2 receptor tyrosine kinase detected by scanning near-field optical microscopy. *Journal of Cell Science* **112**, 1733 (1999).

24 Bag, N., Huang, S. & Wohland, T. Plasma Membrane Organization of Epidermal Growth Factor Receptor in Resting and Ligand-Bound States. *Biophysical journal* **109**, 1925-1936, doi:10.1016/j.bpj.2015.09.007 (2015).

25 Vogel, S. K., Greiss, F., Khmelinskaia, A. & Schwille, P. Control of lipid domain organization by a biomimetic contractile actomyosin cortex. *eLife* **6**, e24350, doi:10.7554/eLife.24350 (2017).

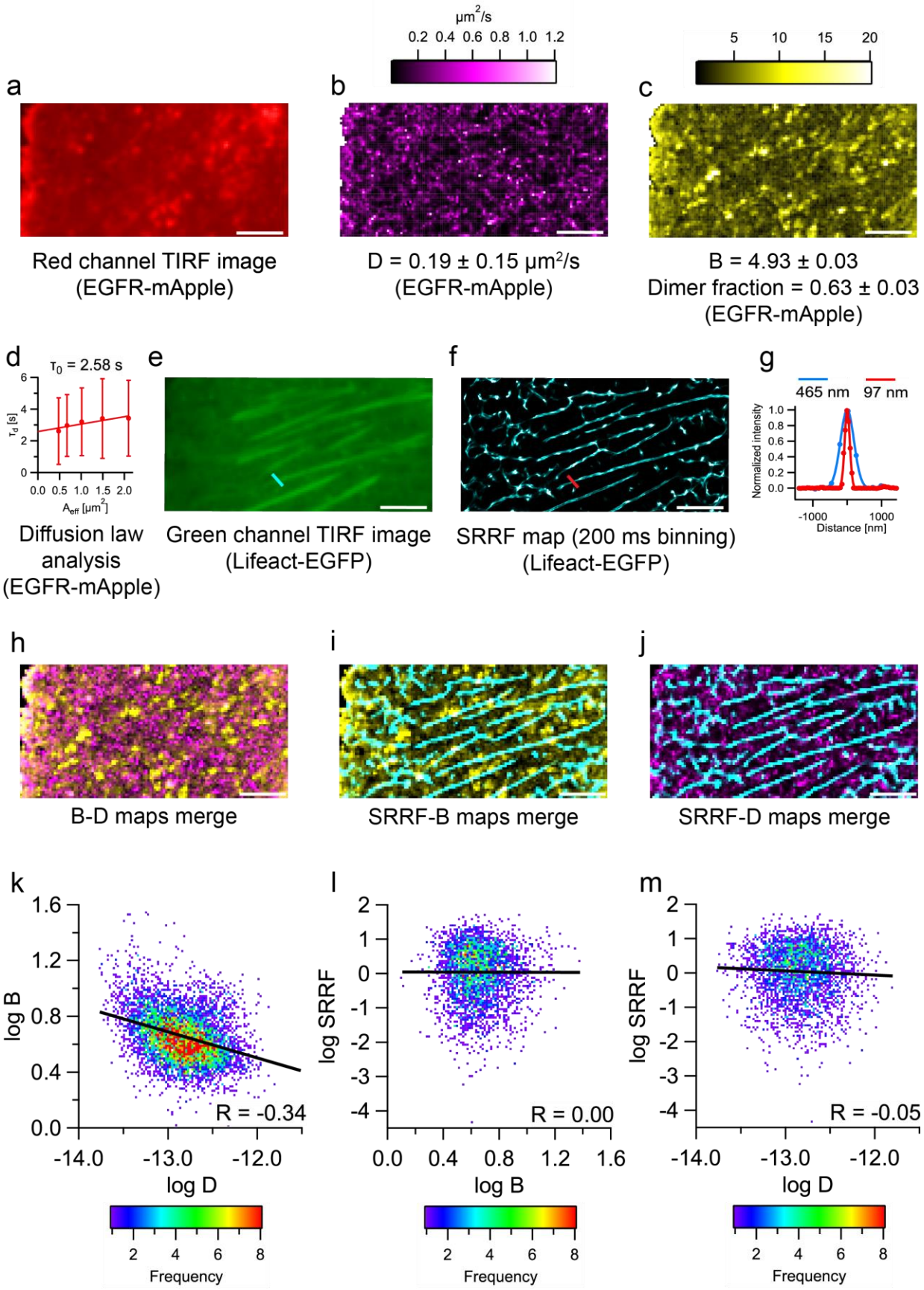
a
b
c
μm²/s
0.2 0.4 0.6 0.8 1.0 1.2
5 10 15 20
Red channel TIRF image
(EGFR-mApple)
D = 0.19 ± 0.15 μm²/s
(EGFR-mApple)
B = 4.93 ± 0.03
Dimer fraction = 0.63 ± 0.03
(EGFR-mApple)
d
τ0 = 2.58 s
τd [s]
Aeff [μm²]
Diffusion law
analysis
(EGFR-mApple)
e
Green channel TIRF image
(Lifeact-EGFP)
f
SRRF map (200 ms binning)
(Lifeact-EGFP)
g
465 nm
97 nm
Normalized intensity
Distance [nm]
h
B-D maps merge
i
SRRF-B maps merge
j
SRRF-D maps merge
k
log B
log D
R = -0.34
l
log SRRF
log B
R = 0.00
m
log SRRF
log D
R = -0.05
Frequency

Fig. 1: Multi-parametric analysis from a single dual-channel fluorescence data set. **(a)** TIRF image of EGFR-mApple. **(b)** Diffusion map of EGFR-mApple (D = 0.19 ± 0.15 μm^2/s). **(c)** Brightness map of EGFR-mApple (B = 4.93 ± 0.03, dimer fraction = 0.63 ± 0.03; mean ± SEM). **(d)** Diffusion law analysis of EGFR-mApple (refer Fig. S10 for more details); intercept = 2.58 s. **(e)** TIRF image of Lifeact-EGFP. **(f)** SRRF map (200 ms binning) of Lifeact-EGFP. **(g)** Normalized intensity profile across an actin fibre before and after SRRF microscopy. Thickness (FWHM of the Gaussian fit) of the actin fibre before SRRF (blue curve) = 465 nm; measurement point marked with blue line on image (e). Thickness of the actin fibre after SRRF (red curve) = 97 nm; measurement point marked with red line on image (f). **(h)** Merge of B and D maps of EGFR-mApple. The B pixels are coloured yellow, and the D pixels are coloured magenta. Correlated pixels between the two maps are coloured white. **(i)** Merge of SRRF (Lifeact-EGFP) and B (EGFR-mApple) maps. SRRF pixels are coloured cyan, and B pixels are coloured yellow. Correlated pixels between the two maps are coloured white. The SRRF map was spatially binned to the same dimensions as the B map. **(j)** Merge of SRRF (Lifeact-EGFP) and D (EGFR-mApple) maps of EGFR-mApple. SRRF pixels are coloured cyan, and D pixels are coloured magenta. Correlated pixels between the two maps are coloured white. The SRRF map was spatially binned to the same dimensions as the D map. **(k)** 2D frequency plot of log B vs log D values from image (h). **(l)** 2D frequency plot of log SRRF vs log B values from image (i). **(m)** 2D frequency plot of log SRRF vs log D values from image (j). The scale bars in white measure 5 μm in images (a)-(e), (h)-(j). This figure uses cell 1 in Table S6. The reported values are averages obtained from analysis of an entire cell.

Online methods

Sample Preparation

CHO-K1 (Chinese Hamster Ovary) cells (CCL-61) were obtained from ATCC (Manassas, Virginia, USA) and were cultured in Dulbecco's Modified Eagle Medium (DMEM/High glucose with L-glutamine, without sodium pyruvate – SH30022.FS; HyClone, GE Healthcare Life Sciences, Utah, USA) supplemented with 1% penicillin-streptomycin (Gibco, Thermo Fisher Scientific, Massachusetts, USA), and 10% fetal bovine serum (FBS; Gibco, Thermo Fisher Scientific, Massachusetts, USA) at 37 °C in a 5% (v/v) CO_2 environment (Forma Steri-Cycle CO_2 incubator, Thermo Fisher Scientific, Massachusetts, USA).

The construction of the plasmids PMT-mApple, PMT-mApple$_2$ and EGFR-mApple are detailed in the supplement. Lifeact-EGFP plasmid was a gift from Prof. Wu Min (NUS, Singapore). All the plasmids were amplified using ZymoPURE II Plasmid Midiprep Kit (D4201; Zymo Research, California, USA) and their concentration and purity were confirmed by a UV-Vis spectrophotometer (NanoDrop 2000, Thermo Fisher Scientific, Massachusetts, USA). The plasmid amounts used for transfection were 100 ng for PMT-mApple, PMT-mApple$_2$ and Lifeact-EGFP, and 1 µg for EGFR-mApple.

For transfection, cell cultures that were ~90% confluent were used. The spent media removed from the culture flask was discarded. The flask was washed twice with 5 ml PBS (phosphate buffered saline; without Ca^{2+} and Mg^{2+}). 2 ml Trypsin-EDTA (0.25%; Gibco, Thermo Fisher Scientific, Massachusetts, USA) was added and the flask was incubated at 37°C for 2-3 minutes to detach the cells. 5 ml culture media was added to the flask to inhibit trypsin. The media containing the detached cells was collected in a falcon tube and centrifuged at 1000 rpm for 3 minutes. The supernatant was discarded and the cell pellet was resuspended in 5 ml PBS. Cell counting was done using a cell counter (Bio-Rad, Singapore). The required number of cells was aliquoted into falcon tubes and centrifuged at 1000 rpm for 3 minutes. The supernatant was discarded and the cells were resuspended in R buffer (Neon Transfection Kit, Thermo Fisher Scientific, Massachusetts, USA). Suitable amounts of Lifeact-EGFP and EGFR-mApple (or PMT-mApple, or PMT-mApple$_2$) (100 ng for Lifeact-EGFP; 1 µg for EGFR-mApple) plasmids were mixed with the cells for co-transfection. The cells were electroporated using Neon Transfection system (Thermo Fisher Scientific, Massachusetts, USA) according to the manufacturer's protocol (electroporation settings: pulse voltage = 1000 V, pulse width = 30 ms, and pulse no. = 2). After transfection, the cells were seeded onto culture dishes (MatTek, Massachusetts, USA) containing DMEM (supplemented with FBS). The cells were incubated at 37°C and 5% CO_2 for 36-48 hours before measurements.

Before EGFR measurements, the cells were washed with HBSS (Hank's Balanced Salt Solution, with Ca^{2+} and Mg^{2+}; #14025134; Gibco, Thermo Fisher Scientific, Massachusetts, USA) and starved in DMEM not containing phenol red (#21063029; Gibco, Thermo Fisher Scientific, Massachusetts, USA) for at least 4 hours. To avoid internalization of EGFR, internalization inhibitors were added to the cells 30 minutes before the measurements. The internalization inhibitors used were 2 mM NaF, 10 mM NaN_3 and 5 mM 2-deoxy-D-glucose (Sigma-Aldrich, Singapore).

Instrumentation

The TIRF microscopy set-up included an inverted epi-fluorescence microscope (IX83, Olympus, Singapore), a motorized TIRF illumination combiner (IX3-MITICO, Olympus, Singapore), and a dual-emission image splitter (OptoSplit II; Cairn Research, Faversham, UK). We used either an electron multiplying charge-coupled device (EMCCD; iXon^{EM}+ 860, 128×128 pixels, Andor, Oxford Instruments, UK) camera or a scientific complementary metal oxide semiconductor (sCMOS; Sona 4.2B-11, Andor, Oxford Instruments, UK) for detection. 488 nm (LAS/488/100, Olympus, Singapore) and 561 nm (LAS/561/100, Olympus, Singapore) lasers were connected to the TIRF illumination combiner. We used a 100X, NA 1.49 oil-immersion objective (Apo N, Olympus) and a magnification changer slider (IX3-MITICO, Olympus, Singapore) to increase magnification two-fold to 200X where required. For the cell measurements, 37°C temperature and 5% CO_2 atmosphere were maintained using an on-stage incubator (Chamlide TC, Live Cell Instrument). The laser power used was 100 µW for the 488 nm laser and 900 µW (EMCCD) for the 561 nm laser (as measured at the back aperture of the objective).

For the dual-channel measurements, the fluorescence light was passed through a dichroic (Di01-R488/561; Semrock) and split by the image splitter on two halves of the camera chip. The image splitter was fitted with an emission dichroic (FF560-FDi01; Semrock) and band-pass filters (510AF23 and 685ALP, respectively; Omega Optical). A bright-field image of a stage micrometer was used to align the image splitter. This was done in µManager (https://micro-manager.org). The image was aligned in both the channels following the manual instructions. To check how good the alignment was, a self-written program in µManager was used to find the similarity in both channels. We considered the channels sufficiently aligned if the similarity was ≥ 95%.In the case of EMCCD, the measurements were done by recording a stack of 50,000 frames of 128×128 pixels at 500 frames per second (fps) (for cell measurements)/1000 fps (for bilayer measurements). Andor Solis was used for image acquisition. The kinetic mode of image acquisition was used and the 'baseline clamp' was always used to minimize the baseline fluctuation. The camera was operated using 10 MHz pixel readout speed. Maximum analog-to-digital gain was set to 4.7 and 0.45 µs vertical shift speed were used. The EM gain used was 300.

Table 1: Acquisition parameters for the various experimental configurations

Camera	Analysis	Laser wavelength [nm]	Time per frame [ms]*	No. of frames	Image pixel size [nm]	Map dimensions [Pixels]
EMCCD	FCS	561	2	50000	240	120×56
Fig.1	Diffusion law	561	2	50000	240	114×56
	N&B	561	20	5000	240	120×56
	SRRF	488	200	500	48	600×280

*: acquisition time was 2 ms; longer times are reached by time binning of frames.

DATA ANALYSES

The data analyses was performed on a computer with the following configuration – Windows 10 Home 64-bit operating system, Intel® Core™ i7-7800X CPU @ 3.50 GHz processor, 32 GB RAM, NVIDIA Titan Xp GPU with 3840 CUDA cores and 12.3 GB memory.

FCS

The image stacks from the cell measurements were loaded in Imaging FCS[27] 1.52 plugin for Fiji and the ACFs calculated. The values used for the parameters were: frame time = 0.002 s, correlator (p, q) = (16, 12), pixel size = 24 µm, NA = 1.49, λ1 = 565 nm (red channel). The EMCCD data analysis was performed at 1×1 binning for 100X magnification. Bleach correction[26] was performed with a polynomial of order 8. ACFs were fitted with a one-component diffusion model.

$$G(t) = \frac{1}{N}\frac{g(t)}{g(0)} \qquad \textit{Eq. 1}$$

$$g(\tau) = \left(\frac{\sqrt{4D\tau + \omega_{xy}^2}}{a\sqrt{\pi}}\left(e^{-\frac{a^2}{4D\tau+\omega_{xy}^2}} - 1\right) + \mathrm{erf}\left(\frac{a}{\sqrt{4D\tau + \omega_{xy}^2}}\right)\right)^2 + G_\infty \qquad \textit{Eq. 2}$$

where a is the pixel size, τ is the lag time, N is the number of particles, D is the diffusion coefficient, ω_{xy} is the PSF (xy) ($1/e^2$ radius) direction. To exclude outliers or non-converged fits, only data with $0.01 < D < 10$ µm^2/s were considered for further analysis.

DIFFUSION LAW

The image stack was analyzed using the Imaging FCS 1.52 plugin for Fiji. The values used for the parameters were: frame time = 0.002 s, correlator (p, q) = (16, 12), pixel size = 24 µm (EMCCD), magnification = 100, NA = 1.49, λ_1 = 565 nm (red channel), PSF (xy) = 0.96 (EMCCD red channel) and bleach correction = polynomial of order 8. In the "Diff. Law" tab, the diffusion law plot was generated and fit with a straight line for square binning 1 to 5 (EMCCD).

N&B

The 2 ms, 50000 frames image stack was temporally binned (sum binning of 10 frames each) to a 20 ms, 5000 frames stack in Fiji. The images were analyzed using the Imaging FCS 1.52 plugin. The values used for the parameters were: frame time = 0.02 s, binning = 1×1 (EMCCD), and bleach correction = polynomial of order 8. An intensity filter with a suitable range was set, as defined by the background intensity in an image, to exclude the background pixels and include only the pixels containing the cell. A dark image (image taken with the camera shutter closed) with the same spatiotemporal dimensions as the measurement image was loaded for background correction in the "Bgr NUM" tab. Then in the "N&B" tab, "G1" was selected in the "NB mode" and the "N&B" button in "N&B analysis" was pressed to generate the N&B maps. The N&B equations are defined as[13]:

$$N = \frac{(\langle I \rangle - \text{ offset})^2}{\sigma^2 - {\sigma_0}^2} \qquad \textit{Eq. 3}$$

$$B = \frac{\sigma^2 - {\sigma_0}^2}{\langle I \rangle - \text{ offset}} \qquad Eq.\ 4$$

where, N is the apparent number of particles in the observation volume, $\langle I \rangle$ is the average intensity, *offset* is the intensity offset of EMCCD, σ^2 is the variance of the signal, B is the apparent brightness of a particle, and σ_0^2 is the variance of the readout noise in the EMCCD. The offset and σ_0^2 can be obtained from a dark image captured by the EMCCD. The variance is typically affected by shot noise, and hence we used the covariance. This is referred to as G1 analysis.

$$\text{Covariance}(F(t), F(t + \Delta t)) = \langle F(t)F(t + \Delta t) \rangle \qquad Eq.\ 5$$

where, $F(t)$ is the fluorescence signal at time t and $F(t+\Delta t)$ is the fluorescence signal at time $t+\Delta t$.

The dimer fraction is determined using the equation below:

$$\text{Dimer fraction} = \frac{r - 1}{2p - r + 1} \qquad Eq.\ 6$$

where r is the ratio of the brightness of EGFR to the brightness of monomer, p is the proportion of the molecules which are fluorescent. The procedure to determine p based on the brightness of monomer and dimer is provided in supplement. The error propagation to estimate the error associated with the dimer fraction is also provided in supplement.

SRRF

The 2 ms, 50000 frames image stack was temporally binned (average binning of 100 frames each) to a 200 ms, 500 frames stack (for Fig. S3 other temporal binnings were also used) in Fiji using the Image → Transform → Bin command sequence. The NanoJ-SRRF[14] plugin was used. The "SRRF analysis" option in the plugin was chosen. The default settings were used, with an addition – the "Do Gradient Smoothing" ("Show Advanced Settings" → "Radiality" → "Do Gradient Smoothing") was also activated. To determine the fibre thickness, the straight line tool in Fiji was used to draw a line segment across a fibre in the generated SRRF maps. The "Plot Profile" function was used to generate an intensity histogram, which was fitted using the "Curve Fitting" tool in Fiji. The curve fitting function used was a Gaussian given by the equation below.

$$y = a + (b - a)e^{\frac{-(x-c)^2}{2d^2}} \qquad Eq.\ 7$$

Where a is the offset, b-a is the height at the centre c, and d is the standard deviation of the Gaussian. The SRRF maps had black borders so the image was cropped to get rid of them. As a result, the original acquired image was cropped before performing FCS, diffusion law and N&B analyses to maintain the same cell area in all the maps (for the image dimensions, refer table 1).

Statistical Analysis

The frequency plots in Fig. 1 were generated using the "*Bivariate histogram*" command in IgorPro© (Wavemetrics Inc, Oregon, USA). A linear fit was performed to estimate the correlation coefficient (*R*). Graphpad Quickcalcs was used to perform t-tests. Only those pixels were included in the scatter plots that had valid values for both parameters.

Code availability

The Imaging FCS 1.52. ImageJ plugin is available at http://www.dbs.nus.edu.sg/lab/BFL/imfcs_image_j_plugin.html or alternatively is included in the ImageJ update site.

Data availability

The datasets generated during the current study are available from the corresponding author on reasonable request.

Competing Interests

The authors declare that there are no competing interests.

References

26 Macháň, R., Foo, Y. H. & Wohland, T. On the Equivalence of FCS and FRAP: Simultaneous Lipid Membrane Measurements. *Biophysical journal* **111**, 152-161, doi:10.1016/j.bpj.2016.06.001 (2016).

27 Sankaran, J., Shi, X., Ho, L. Y., Stelzer, E. H. & Wohland, T. ImFCS: a software for imaging FCS data analysis and visualization. *Optics express* **18**, 25468-25481, doi:10.1364/oe.18.025468 (2010).